

where $\lambda_1 = 4\pi^2\nu_1^2$ and k_{12} is the coupling force constant. The results for CrH₂ and MoH₂ are listed in Table V together with the stretching force constants.

Conclusions

In a summary, the reaction patterns for both chromium and molybdenum atoms with molecular hydrogen in Kr and Ar matrices have been found to be extremely similar presumably due to their similar electronic configurations. A larger stretching force constant and a smaller bond angle for MoH₂ than for CrH₂ have

been observed. The unexpected splitting in the stretching modes of MHD molecules, which has not been observed for any other unligated metal dihydrides, suggests that a small difference exists in the bond distances for M-H and M-D bonds in the MHD(Cr, Mo) species. It would be of interest to explore this possibility theoretically, since the presence of inequivalent bonds requires that a double minimum exists for each bond.

Acknowledgment. This work has been supported by the Robert A. Welch Foundation and by MSNW, Inc.

Reaction Potential Surface for $B^+(^1S) + H_2 \Rightarrow HBH^+(^1\Sigma_g^+)$, $BH^+(^2\Sigma) + H(^2S)$

Jeff Nichols,[†] Maciej Gutowski, Samuel J. Cole,[†] and Jack Simons*

Chemistry Department, University of Utah, Salt Lake City, Utah 84112 (Received: July 9, 1991)

The reaction of $B^+(^1S)$ with H_2 on the ground potential energy surface is examined using ab initio electronic structure methods. In the entrance channel, a weakly bound T-shaped $B^+\cdots H_2$ complex of C_{2v} symmetry is found to lie 422 cm⁻¹ below the $B^+ + H_2$ reactant energy. Its H-H internuclear distance is only slightly distorted from that of H_2 ; the B-H distance (ca. 2.6 Å) is much longer than the covalent bond length in BH^+ (1.2 Å). Further along the reaction coordinate is found a narrow valley characterized by strong B^+ -to- H_2 interreactant forces but very small distortion of the H-H bond length or the H-H vibrational frequency. Further up the floor of this valley, a geometry is reached at which, through second-order Jahn-Teller coupling, the asymmetric motion (of b_2 symmetry) develops negative curvature and thus becomes geometrically unstable. From this point of instability, distortion along the asymmetric mode can lead directly to the $BH^+(^2\Sigma) + H$ products. The energy of this instability point is 22 842 cm⁻¹ above $B^+ + H_2$ and 2021 cm⁻¹ or ca. 0.25 eV above the thermodynamic reaction threshold for $BH^+ + H$ formation, which is predicted to be 20 000 cm⁻¹. In addition, a geometrically stable linear $HBH^+(^1\Sigma_g^+)$ species is found to lie 14 712 cm⁻¹ below $B^+ + H_2$. Its BH bond length ($r_{BH} = 1.187$ Å) is only slightly shorter than that in BH^+ (1.199 Å). All of these findings are in reasonable agreement with known experimental data on the reactivity of B^+ with H_2 . However, another (collinear) reaction path has been found that leads to $BH^+(^2\Sigma) + H$ without any barrier above the thermodynamic requirement; this path, if operative, is not consistent with experimental findings. A proposal is offered to explain how the path that passes through the point of instability may be of more relevance to the guided-ion beam data than the lower energy collinear path.

I. Introduction

(A) **Why Study $B^+(^1S) + H_2$?** The present work was undertaken to provide theoretical interpretation for experimental guided ion beam and other data¹ on the $B^+ + H_2 \Rightarrow BH^+ + H$ reaction. The ion beam experiments give the cross section for $(^2\Sigma)BH^+$ production as a function of B^+ kinetic energy and show a threshold energy for BH^+ production that exceeds the endothermicity of the reaction. The origin of this activation energy was a primary inspiration for this study. As shown in section IV, we conclude that the majority of the collisions occurring at energies characteristic of the ion-beam experiments proceed through a near- C_{2v} B^+H_2 structure which lies ca. 0.25 eV above the $BH^+ + H$ products and which reaches the $BH^+ + H$ product channel because of instability in its asymmetric b_2 distortion mode. What is surprising is that this conclusion is reached even though there exists a collinear path connecting $B^+ + H_2$ to $BH^+ + H$ that has no activation barrier in excess of the reaction endoergicity.

(B) **Earlier Related Studies and Characteristics of Similar Potential Surfaces.** Earlier theoretical calculations² on $Be(^1S) + H_2 \Rightarrow HBeH(^1\Sigma_g)$ and on $^3Mg(^1S) + H_2 \Rightarrow HMgH(^1\Sigma_g)$ yielded qualitatively similar ground-state 1A_1 , C_{2v} -constrained potential energy surfaces. The findings of these studies were expected to guide us in the present work and therefore merit consideration.

A two-dimensional contour characterization of the $Be + H_2$ ground-state surface is given in Figure 1; the variation of the

TABLE I: Electronic States Energies (eV) for Reactants and Products Measured with Respect to $B^+(^1S) + H_2(X^1\Sigma_g^+)$

reactants ^a		products ^b	
$B^+(^1S) + H_2(^1\Sigma_g^+)$	0.0	$BH^+(X^2\Sigma^+) + H(^2S)$	2.6
$B^+(^3P) + H_2(^1\Sigma_g^+)$	4.6	$BH^+(A^2\Pi) + H(^2S)$	5.1
$B(^2P) + H_2(^2\Sigma_g^+)$	8.0	$BH(X^1\Sigma^+) + H^+$	7.1
$B^+(^1P) + H_2(^1\Sigma_g^+)$	9.1	$BH^+(B^2\Sigma^+) + H(^2S)$	10.0

^a B^+ energies obtained from Atomic Energy Levels. Moore, C. E. *Nat. Stand. Ref. Data Ser., Nat. Bur. Stand. (U.S.)* 1971, 34/V.I. H_2^+/H_2 energies obtained from ab initio calculation. ^b Based on calculated results from the present work.

energy along the asymmetric distortion mode is not depicted in this figure, although in these earlier works attention was paid to points at which motion along the asymmetric direction was geometrically unstable. The surface of Figure 1 clearly shows a narrow entrance channel (labeled a) along which Be approaches an essentially intact H_2 molecule, a region in which H-H motion

(1) (a) Armentrout, P. B. *Int. Rev. Phys. Chem.* 1990, 9, 115. Elkind, J. L.; Armentrout, P. B., unpublished results. Ruatta, S. A.; Hanley, L.; Anderson, S. L. *J. Chem. Phys.* 1989, 91, 226. (b) Rosmus, P.; Klein, R. Thesis by Klein, University of Frankfurt, 1984. (c) Schneider, F.; Züllicke, L.; Polak, R.; Vojtik, J. *J. Chem. Phys. Lett.* 1984, 103, 608. (d) Lin, K. C.; Watkins, H. P.; Cotter, R. J.; Koski, W. S. *J. Chem. Phys.* 1974, 56, 1003. Ruatta, S. A.; Hanley, L.; Anderson, S. L. *J. Chem. Phys.* 1989, 91, 226.

(2) O'Neal, D.; Taylor, H.; Simons, J. *J. Phys. Chem.* 1984, 88, 1510.

(3) Adams, N.; Breckenridge, W. H.; Simons, J. *J. Chem. Phys.* 1981, 56, 327.

(4) Herzberg, G. *Atomic Spectra and Atomic Structure*; Dover Publications: New York, 1944; p 200.

[†] Utah Supercomputer Institute/IBM Corporation Partnership, Salt Lake City, UT 84112.

* Permanent address: CAChE Group, Tektronix, Inc., P.O. Box 500 M.S. 13-400, Beaverton, OR 97077.

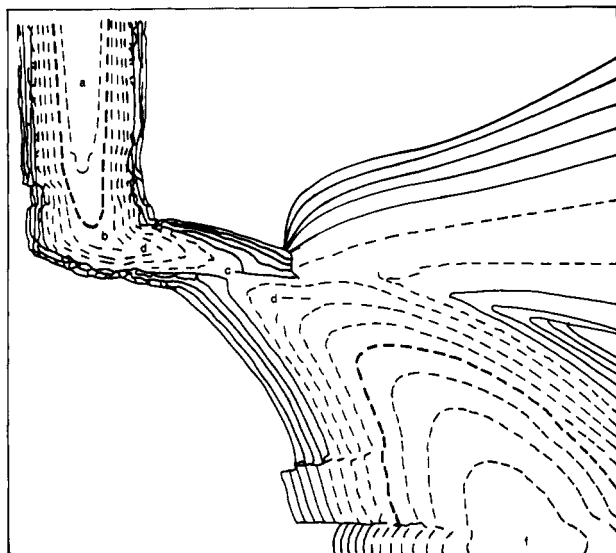


Figure 1. Two-dimensional contour plot of the ground-state 1A_1 potential energy surface for the C_{2v} insertion of $\text{Be}(^1S)$ into H_2 to produce linear $\text{HBeH}(^1\Sigma)$. The contour spacings represent approximately 5000 cm^{-1} in energy. Along the vertical axis is the distance from the Be^+ to the center of the H-H bond; the horizontal axis labels the H-H distance. The labels a-d, f refer to the geometrical points discussed in section I.B.

begins to play a role (point b), a saddle point (point c), and two exit valleys leading, respectively, to $\text{H} + \text{Be} + \text{H}$ (to the right of point c) and HBeH (point f) products.

The reaction that produces $\text{BeH} + \text{H}$ products cannot be represented in Figure 1 because of the artificial C_{2v} symmetry constraint. However, by monitoring where the asymmetric (b_2) distortion mode achieves negative curvature (points d) and thus becomes unstable, or where the lowest surface of 1B_2 symmetry intersects the 1A_1 surface and thus allows transitions to the 1B_2 surface to occur, one can determine at what energy the $\text{BeH} + \text{H}$ product channel becomes accessible. To achieve a full picture of all product channels therefore dictates that the position of the 1B_2 surface relative to the 1A_1 surface be carefully monitored.

Both of the above alkaline-earth-metal atoms as well as the analogous B^+ ion considered here have $ns^2\ ^1S$ ground electronic states and relatively low-lying $nsnp\ ^1P$ excited states. It is these states that contribute strongly to the 1A_1 and 1B_2 surfaces that must be examined. Among the alkaline-earth-metal atoms and B^+ , the energies of the 1P atomic states relative to the 1S ground state as well as the strengths of the metal-H bonds vary considerably. Moreover, in the $\text{B}^+ + \text{H}_2$ case, states arising from the $\text{B}(^2P) + \text{H}_2^+$ asymptote lie below the $\text{B}(^1P) + \text{H}_2$ energy and thus must also be taken into account (see Table I).

Before discussing our findings, let us anticipate some of the electronic structure characteristics that would be expected to affect strongly the dynamics^{1a-c} (e.g., energy threshold, cross-section magnitude, and energy dependence) of the $\text{B}^+ + \text{H}_2$ reaction which is the focus of this work. This discussion helps establish requirements that we need to place on the computational approaches used to achieve the potential surfaces presented here.

(C) C_{2v} Symmetry: $\text{M} + \text{H}_2$ Reactants, $\text{H} + \text{M} + \text{H}$, and HMH Products. (1) Orbital Symmetry Labels. We begin by defining the C_{2v} symmetry notation used to label the molecular orbitals of the various species. For the $\text{M} + \text{H}_2$ reactants, the labels $1a_1$, $2a_1$, and $1b_2$ are used to denote the valence $\text{H}_2\ \sigma_g$, $\text{M}\ ns$, and M (in plane and parallel to the H-H axis) np orbitals, respectively. The $3a_1$ and $1b_1$ orbitals are the other two $\text{M}\ np$ orbitals; the $\text{H}_2\ \sigma_u$ antibonding orbital is denoted $2b_2$. The M inner-shell orbitals are not explicitly identified in this abbreviated notation.

For the linear HMH product molecule, $1a_1$, $2a_1$, and $1b_2$ denote the $\text{M-H}\ \sigma$, σ^* , and σ orbitals, respectively; the $2b_2$ orbital is another $\text{M-H}\ \sigma^*$ orbital. The π -orbitals of the HMH molecule are labeled $1b_1$ and $3a_1$.

When considering the $\text{H} + \text{M} + \text{H}$ channel again in C_{2v} symmetry, the symmetric combination of the two $\text{H-atom}\ 1s$ orbitals

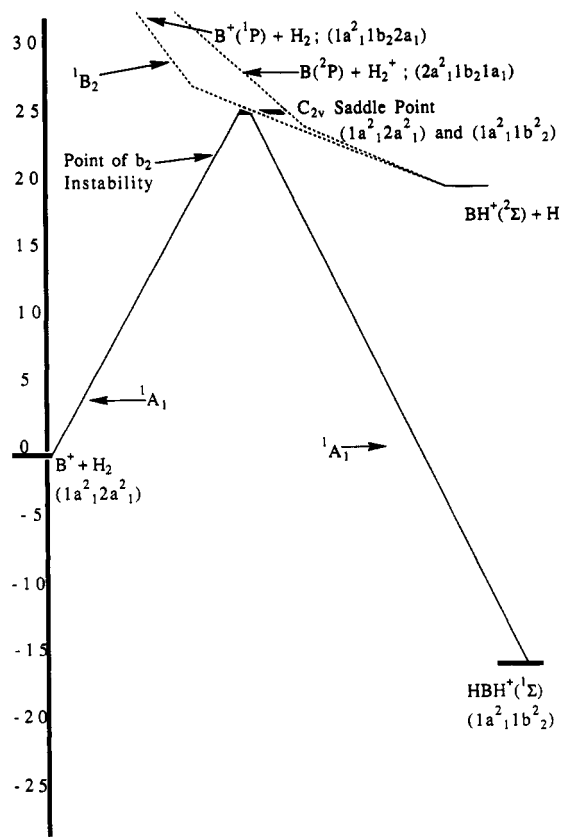


Figure 2. Configuration correlation diagram for C_{2v} insertion of $\text{B}^+(^1S)$ into H_2 to produce linear HBH^+ . The energies are in units of 1000 cm^{-1} . The $1a_1$, $2a_1$, and $1b_2$ orbitals correspond to the $\text{H}_2\ \sigma_g$, $\text{B}^+(2s)$, and $\text{B}^+(2p)$ (in plane) orbitals, respectively for the $\text{B}^+ + \text{H}_2$ reactants. For the HBH^+ product, the $1a_1$ and $1b_2$ orbitals are the two (symmetric and asymmetric) $\sigma\ \text{B-H}$ bonding orbitals.

is labeled $2a_1$, the antisymmetric combination is labeled $1b_2$, the $\text{M}\ ns$ orbital is denoted $1a_1$, and the three $\text{M}\ np$ orbitals are $3a_1$, $1b_1$, and $2b_2$.

Notice that in all three of the above cases there are a total of six orbitals explicitly considered; when C_s and $C_{\infty v}$ symmetries are considered, again a total of six important orbitals will occur. This is an essential fact to keep in mind when designing our calculational approach.

(2) Essential Electronic Configurations. The need for using an inherently multiconfigurational approach when treating the ground-state potential surfaces that arise here can now be made clear. Briefly, the valence ns^2 configuration of the reactant M atom (or ion) when combined with the σ_g^2 configuration of the H_2 molecule in its $X\ ^1\Sigma_g^+$ ground state, does not correlate with the ground-state $\sigma_g^2\ \sigma_u^2$ dominant configuration of the linear HMH molecule (or ion). In C_{2v} symmetry, the $\text{M} + \text{H}_2$ reactants have the $\sigma_g^2\ ns^2 = 1a_1^2 2a_1^2$ electronic configuration, and, as stated, the HMH products have the $\sigma_g^2\ \sigma_u^2 = 1a_1^2 1b_2^2$ configuration. Although both configurations are of 1A_1 symmetry, they are not identical; this means that the electronic wavefunction changes its qualitative character (i.e., orbital occupancy) in moving from reactants to products.

For collisions that produce $\text{H} + \text{M} + \text{H}$ along a path preserving C_{2v} symmetry, two configurations of the form $1a_1^2 2a_1^2$ and $1a_1^2 1b_2^2$ are needed. By combining these two configurations, the homolytic dissociation of the two H atoms can be achieved, just as combining σ_g^2 and σ_u^2 configurations is needed to describe homolytic dissociation of H_2 .

It is therefore clear that at least two electronic configurations are needed to describe the $\text{M} + \text{H}_2$ reactants and the $\text{H} + \text{M} + \text{H}$ or HMH products in C_{2v} symmetry. For these reasons, a multiconfigurational wave function must be used. These configuration correlations are summarized semiquantitatively in Figure 2 where the relative positions of the low-lying B_2 states are also anticipated.

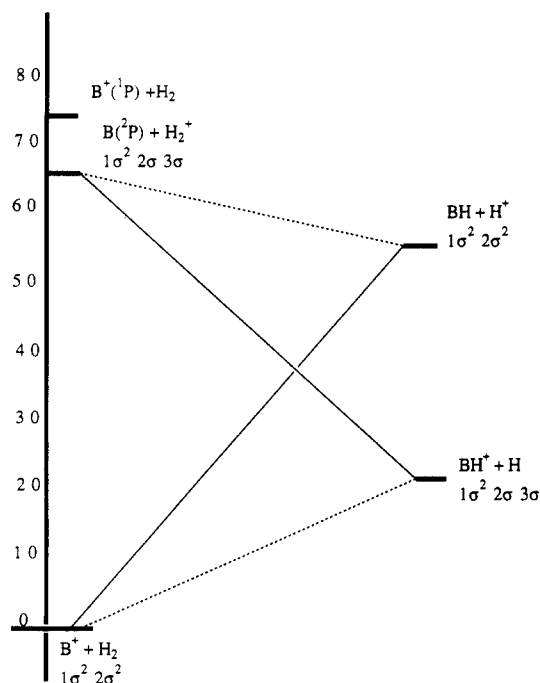


Figure 3. Configuration correlation diagram for collinear insertion of $B^+(^1S)$ into H_2 to produce $BH^+(^2S) + H$. The energies are in units of 1000 cm^{-1} . The 1σ , 2σ , and 3σ orbitals correspond to the H_2 σ_g , B^+ $2s$ and B^+ $2p$ (along the molecular axis) orbitals, respectively for the $B^+ + H_2$ reactants. For $BH^+ + H$, 1σ is the BH^+ σ bonding orbital, 2σ is the BH^+ nonbonding σ orbital, and 3σ is the H atom $1s$ orbital. The solid lines show the diabatic configuration correlations, and the dashed lines show the adiabatic state correlations in which no avoided crossing occurs.

It still remains to determine which, if any, additional configurations must be included to describe the $MH + H$ products that arise when C_{2v} symmetry is broken or when considering collinear approaches of B^+ to H_2 .

(D) Including C_s and $C_{\infty v}$ Symmetry Paths. When the C_{2v} symmetry is lowered to C_s symmetry, the a_1 and b_2 orbitals become orbitals of the same a' symmetry. The $1a_1$, $2a_1$, $1b_2$, $3a_1$, and $2b_2$ orbitals become $1a'$, $2a'$, $3a'$, $4a'$, and $5a'$, whereas the $1b_1$ orbital becomes the $1a''$ orbital. The $MH + H$ product channel can be described in this symmetry where the ground-state $MH(^2\Sigma) + H$ species have a dominant $1a'^2 2a' 3a'$ configuration ($1a'$ is the $M-H$ σ -bonding orbital, $2a'$ is the H -atom $1s$, and $3a'$ is the nonbonding σ orbital on the MH).

In $C_{\infty v}$ symmetry, the corresponding six active orbitals have σ (the M ns and one np as well as the H_2 bonding and antibonding orbitals) and π (two of the M np orbitals) symmetries. As in all of the other symmetries, there are a total of six explicitly labeled orbitals. Within the $C_{\infty v}$ point group, the $M + H_2$ species have a dominant $1\sigma^2 2\sigma^2$ configuration, and the $MH + H$ species have a dominant $1\sigma^2 2\sigma 3\sigma$ configuration (see Figure 3).

(E) Complete-Active-Space List of Configurations. We can achieve a balanced description of the $M + H_2$, $H + M + H$, HMH , and $MH + H$ channels by including in the electronic wave function all configurations of a chosen overall symmetry (e.g., 1A_1 or $^1A'$) with the four valence electrons distributed among all six "active" orbitals in all ways that produce the chosen overall symmetry. Doing so is said to involve a complete-active-space (CAS) description of the electronic configuration space.

This choice of configurations allows us to include in our ground-state wave function not only the dominant configurations appropriate to $M(^1S) + H_2$, $HMH(^1\Sigma_g^+)$, $H + M(^1S) + H$, and $MH(^2\Sigma) + H$ but also those configurations that correlate with low-lying excited asymptotic $^1A'$ state such as $B^+(^1^3P) + H_2$, $BH(^1\Sigma) + H^+$, and $B(^2P) + H_2^+$. It also allows us to study the low-energy states of $^1,^3B_2$ symmetry that arise from various of these asymptotes as discussed in the next sections.

(F) Role of Low-Energy Excited Configurations. The configurations that result from distributing the four valence electrons

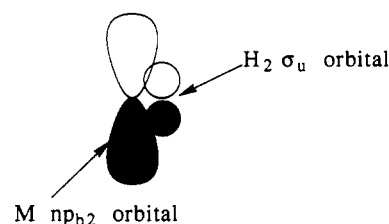


Figure 4. Constructive interaction between the in-plane M np orbital of b_2 symmetry and the antibonding H_2 σ_u orbital also of b_2 symmetry.

among the active orbitals in all manner consistent with the chosen symmetry involve both open-shell configurations of the type $1a'^2 2a' 3a'$ and closed-shell configurations such as $1a'^2 2a'^2$ and $1a'^2 1a''^2$. The couplings among these configurations determine the nature of the electronic energy surfaces as functions of geometry. Whenever configurations that differ by the occupancy of two spin-orbitals interact (e.g., $1a'^2 2a'^2$ and $1a'^2 1a''^2$), the coupling is rather weak, and an avoided crossing barrier is to be expected. When two configurations that differ by a single spin-orbital occupancy interact (e.g., $1a'^2 2a'^2$ and $1a'^2 2a' 1a''$), the coupling is strong and an avoided crossing barrier is likely to not appear. Such considerations are, of course, conceptually useful, but whether a transition-state barrier appears must be determined by *ab initio* calculations.

The excited $^1,^3P$ states of the B^+ species, when interacting with H_2 in C_{2v} symmetry, give rise to singlet and triplet states of A_1 , B_1 , and B_2 symmetry. Also, singlet and triplet A_1 , B_1 , and B_2 states result from the interaction of neutral $B(^2P)$ and H_2^+ , which lies below $B^+(^1P) + H_2$ by approximately 1 eV .

Among the excited A_1 , B_1 , and B_2 states, the $^1,^3B_2$ states possess the most attractive interactions because they allow the B^+ in-plane half-filled np orbital of b_2 symmetry to interact constructively with the H_2 molecule's empty antibonding σ_u orbital as shown in Figure 4. Earlier work on $Be + H_2$ and $Mg + H_2$ led us to anticipate that the 1A_1 ($^1A'$) ground-state surface will either be intersected or closely approached by the lowest $^1,^3B_2$ ($^1,^3A'$) surfaces. If so, there are important consequences for the reaction under discussion.

In particular, collisions entering regions where the 1A_1 and 1B_2 surfaces cross may "hop" from one surface to the other since any loss of C_{2v} symmetry permits the 1A_1 and 1B_2 states to mix. Once on the 1B_2 surface the reaction can proceed directly to the $MH(^2\Sigma) + H$ products. Of course, if any appreciable spin-orbit coupling is operative, hopping to the 3B_2 surface, which also correlates directly to the $MH(^2\Sigma) + H$ products, can also occur.

If the 1A_1 and 1B_2 surfaces do not cross yet approach closely, $MH + H$ products can still be formed. In this case, the mechanism involves second-order Jahn-Teller coupling between the underlying 1A_1 surface and the higher 1B_2 surface induced by a distortion of b_2 symmetry. If the strength of such coupling is sufficiently strong, instability with respect to distortion along the b_2 mode will develop on the 1A_1 surface. The BH_2^+ species will spontaneously distort when reaching such points of instability on the 1A_1 surface, and subsequently evolve to $BH^+ + H$ on the (now) $^1A'$ surface in C_s symmetry.

The strength of the factors that produce negative curvature and thus instability along the b_2 mode is governed by matrix elements of the form⁵

$$\frac{|\langle ^1A_1 | \partial H / \partial Q_{b_2} | ^1B_2 \rangle|^2}{(E(^1A_1) - E(^1B_2))}$$

where $\partial H / \partial Q_{b_2}$ represents the derivative of the electronic Hamiltonian with respect to distortion along the b_2 mode. The closer the 1B_2 state approaches the underlying 1A_1 state, the larger is this negative-curvature factor. If the 1B_2 state intersects and moves below the 1A_1 state, this factor ceases to produce negative curvature along the b_2 mode; however, in this case, straightforward hopping to the 1B_2 surface can occur without second-order Jahn-Teller assistance.

(5) Simons, J. *Energetic Principles of Chemical Reactions*; Jones and Bartlett Publishers: Boston, 1983.

TABLE II: Total and Relative Energies, Geometries, and Vibrational Frequencies for Species along the $B^+ + H_2 \rightarrow BH^+ + H$, $BH^+ + H$, $BH^+ + H$ Reaction Paths^a

species	method used	electronic energies, hartrees	optimized geometries, Å	vibr frequencies ^c / zero-point energies, cm ⁻¹	rel energies, ^b cm ⁻¹
$B^+(^1S) + H_2$	MCSCF	-25.446 250	$r_{HH} = 0.755$	4224/2112	
	CCSD(T)	-25.468 865	$r_{HH} = 0.734$		0
$BH_2^+ C_{2v}$ long-range complex	MCSCF	-25.449 485	$r_{HH} = 0.762$; $r_{BH} = 2.605$	230 (a ₁), 437 (b ₂), 4133 (a ₁)/2400	-710
	CCSD(T)	-25.474 069	$r_{HH} = 0.743$; $r_{BH} = 2.605$		
$BH_2^+ C_{2v}$ second-order saddle point	MCSCF	-25.322 627	$r_{HH} = 1.396$; $r_{BH} = 1.411$	4512i (a ₁), 1279 (a ₁), 3424i (b ₂) ^d	27 129
	CCSD(T)	-25.352 230			
$BH^+(^1\Sigma)$	MCSCF	-25.520 364	$r_{BH} = 1.187$	2594 (a ₁), 2880 (b ₂), 932 (bend)/3669	-16 269
	CCSD(T)	-25.563 931			
	CCSD(T)	-25.564 067	$r_{BH} = 1.173$		
$BH_2^+ C_{2v}$ point of b ₂ mode instability	MCSCF	-25.342 173	$r_{HH} = 1.336$; $r_{BH} = 1.526$		22 842
$BH^+(^2\Sigma) + H$	MCSCF	-25.351 373	$r_{BH} = 1.199$	2582/1291	20 821
	CCSD(T)	-25.371 722	$r_{BH} = 1.198$		
BHH^+ linear complex	MCSCF	-25.446 663	$r_{HH} = 0.756$; $r_{BH} = 2.729$	112, 4202, 303i (bend) ^d /2157	-91
	CCSD(T)	-25.469 942			
	CCSD(T)	-25.488 630	$r_{HH} = 0.702$; $r_{BH} = 2.865$		

^a Where separate geometry optimizations were carried out at the MCSCF and CCSD(T) levels, two sets of geometries are reported. In all cases, the MCSCF geometry is listed first, and the CCSD(T) geometry appears second. Where geometry optimization could not be carried out at the CCSD(T) level, the CCSD(T) energies were computed at the MCSCF geometries. ^b In all cases, the MCSCF energies are used and are given relative to the $B^+ + H_2$ reactants. These are electronic energies, and thus do not include zero-point corrections. ^c These local harmonic frequencies were obtained from the analytical second derivatives of the MCSCF energy at the MCSCF geometries. ^d It is not appropriate to compute zero-point energies here because this is neither a true minimum nor transition state.

II. Computational Methods

(A) **Basis Sets.** The basis set for the H atoms consists of the Dunning augmented correlation consistent (cc) polarized valence triple- ζ (p-VTZ) [5s2p1d|3s2p1d] set⁶ of functions. For the B^+ ion, the Dunning [10s5p2d|4s3p2d] augmented cc p-VTZ basis set was used. A total of 55 contracted Gaussian-type basis functions resulted.

(B) **Electronic Configurations and Wave Functions.** Both CAS-based multiconfigurational self-consistent field (MCSCF) and coupled-cluster methods were used to treat correlations among the four valence electrons of the BHH^+ system. In particular, the CCSD(T) variant⁷ of the coupled-cluster approach,⁸ which includes all single and double excitations in a fully correct manner and treats triple excitations by approximate noniterative means, was employed.

The discussion of section I makes it clear that no single electronic configuration can describe even the ground state of this system throughout the C_{2v} , $C_{\infty v}$, or C_s reaction paths. For this reason, multiconfigurational methods were required. In the MCSCF calculations, the four valence electrons were distributed, in all ways consistent with overall spatial and spin symmetry, among the six valence orbitals whose symmetries and physical natures were discussed in section I. This process generated 41 electronic configurations of 1A_1 symmetry in the C_{2v} point group and 65 of $^1A'$ symmetry in the C_s point group; it yielded 41 configurations in the $C_{\infty v}$ group.

The above MCSCF calculations were employed, along with our Utah MESSKit⁹ analytical energy derivative and potential energy surface "walking" algorithms¹⁰ to find and characterize (via ge-

ometry and local harmonic vibrational frequencies) the local minima, transition states, and reaction paths discussed below. Although our own algorithms were used to effect "uphill" movements on the energy surfaces, a steepest descent¹¹ method was employed to move "downhill" from critical points toward local minima. The latter approach allowed us to more accurately identify important points on the surface. Near critical points or points of surface intersection, the CCSD(T) method was used to evaluate the total correlation energies to provide a "check" on our MCSCF data. Moreover, finite difference methods were employed within the CCSD(T) approach to further verify the predicted geometries of such critical points on the surface.

III. Findings and Comparison to Guided-Ion Beam Results

As detailed in Table II and described qualitatively in Figures 2 and 3, we find the potential energy surface for $B^+(^1S) + H_2 \rightarrow BH^+(^2\Sigma) + H$ to possess most of the features expected from the discussion in sections I and II and to display many of the same features of our earlier $Be + H_2$ and $Mg + H_2$ surfaces. However, there are new features that result from the ionic character of this system. For example, the long-range interactions are much stronger than in the neutral species, and they favor C_{2v} rather than collinear approaches. Moreover, because the 1P state of B^+ lies much higher than the corresponding state of Be or Mg , the 1B_2 state does *not* intersect the 1A_1 state during the C_{2v} insertion, although it closely approaches the 1A_1 state over a substantial range of geometries. This, in turn through second-order Jahn-Teller coupling, causes the region over which the b_2 asymmetric distortion mode is geometrically unstable to be larger than in the Be and Mg cases.

Our primary findings as they relate to the $B^+ + H_2$ case at hand are summarized as follows:

(a) As the B^+ ion approaches the H_2 molecule from very long range (e.g., $R = 25$ Å or further), the charge-quadrupole interaction (which varies as R^{-3}) favors a "T-shaped" C_{2v} approach and produces a narrow reaction path valley. In this long-range region, a linear structure is made unstable with respect to bending by the quadrupole force. As one moves up this valley to smaller R values, the charge-induced dipole interaction (which varies as R^{-4}) comes into play. This factor favors approach of an ion along the H-H axis (because $\alpha_{||} = 0.934$ Å³ > $\alpha_{\perp} = 0.718$ Å³). However, the R^{-3} electrostatic interaction dominates and the valley

(6) Dunning, T. *J. Chem. Phys.* **1989**, *90*, 1007.

(7) Raghavachari, K.; Trucks, G. W.; Pople, J. A.; Head-Gordon, M. *Chem. Phys. Lett.* **1989**, *157*, 479.

(8) Cizek, J. *J. Chem. Phys.* **1966**, *45*, 4256; *Adv. Chem. Phys.* **1969**, *14*, 35. Cizek, J.; Paldus, J. *Int. J. Quantum Chem.* **1971**, *5*, 359. Bartlett, R. *J. J. Phys. Chem.* **1989**, *93*, 1697, for a recent comprehensive review of developments in this field.

(9) The Utah MESSKit is a suite of highly modular codes that were programmed in-house to give a variety of electronic structure functionalities by J. A. Nichols, M. R. Hoffmann, R. A. Kendall, H. L. Taylor, D. W. O'Neal, E. Earl, R. Hernandez, M. Gutowski, J. Boatz, K. Bak, J. Anchell, X. Wang, M. Feyerisen, and J. Simons.

(10) Nichols, J.; Taylor, H.; Schmidt, P.; Simons, J. *J. Chem. Phys.* **1990**, *92*, 340. Simons, J.; Jorgensen, P.; Taylor, H.; Ozment, J. *J. Phys. Chem.* **1983**, *87*, 2745. O'Neal, D.; Taylor, H.; Simons, J. *J. Phys. Chem.* **1984**, *88*, 1510. Banerjee, H.; Adams, N.; Simons, J.; Shepard, R. *J. Phys. Chem.* **1985**, *89*, 52. Taylor, H.; Simons, J. *J. Phys. Chem.* **1985**, *89*, 684. Cerjan, C. J.; Miller, W. H. *J. Chem. Phys.* **1981**, *75*, 2800. Baker, J. *J. Comput. Chem.* **1988**, *9*, 465. Baker, J. *J. Comput. Chem.* **1986**, *7*, 385.

(11) Fukui, K. *J. Phys. Chem.* **1970**, *74*, 4161.

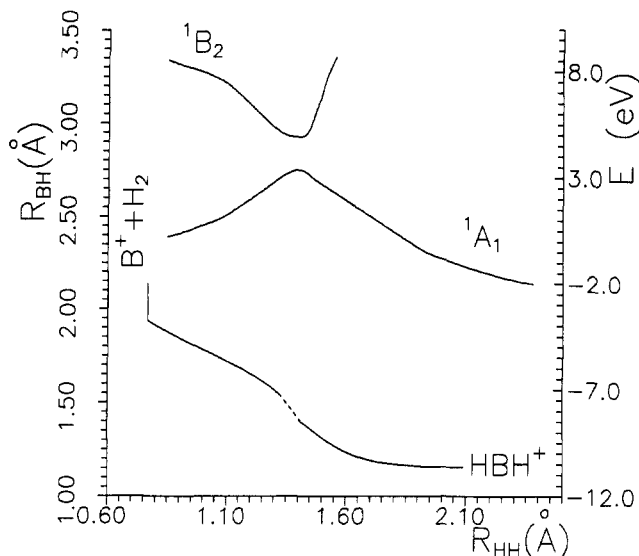


Figure 5. Reaction path for C_{2v} insertion. The lower curve gives the HH and BH distances along this path. The region of b_2 mode instability resulting from coupling between 1A_1 and 1B_2 electronic states is depicted by a dashed line. The upper two curves show the 1A_1 and 1B_2 energies (measured with respect to reactants $B^+ + H_2$) along this path.

eventually leads to a T-shaped C_{2v} complex.

(b) This weakly bound $B^+ \cdots H_2$ complex lies 710 cm^{-1} below the $B^+ + H_2$ reactant energy. When zero-point corrected, this complex is stable by only 422 cm^{-1} . At this geometry, the effects of basis set superposition error were checked at the MCSCF level and found to be only 3.8 cm^{-1} . This complex has a structure in which the H–H internuclear distance is only slightly distorted from that of H_2 ; the B–H distance (ca. 2.6 \AA) is much longer than the covalent bond length in BH^+ (1.2 \AA). Further along the reaction coordinate, the valley is characterized by stronger and stronger B^+ -to- H_2 interreactant forces but very small distortion of the H–H bond length or the H–H vibrational frequency.

(c) As one proceeds further up the valley, a geometry is reached at which the asymmetric distortion mode (of b_2 symmetry) develops negative curvature (see Figure 5) at which the reaction can proceed without further energy constraint to $BH^+({}^2\Sigma) + H$. This point of instability occurs at an (MCSCF) energy $22\,842 \text{ cm}^{-1}$ above the $B^+ + H_2$ reactants, an HH distance of 1.336 \AA and a BH distance of 1.526 \AA . It lies 2021 cm^{-1} or ca. 0.25 eV above the thermodynamic reaction threshold, which corresponds approximately to where the guided ion beam experiments first detect production of BH^+ product ions.

(d) Even further along the C_{2v} -constrained path, a stationary point is reached at which negative curvature exists along one of the two a_1 symmetric distortions and along the b_2 asymmetric mode. As such, this second-order saddle point is not a true transition state; it would be a transition state if the reaction were constrained to C_{2v} symmetry. The negative curvature of the b_2 mode persists from the point of instability described above, through this second-order saddle point, and beyond as a consequence of the second-order Jahn–Teller coupling between the ground 1A_1 state and the 1B_2 state. Since the 1B_2 state lies above the 1A_1 state throughout this entire region, the negative b_2 curvature persists throughout this region. Eventually, beyond the second-order saddle point, as the BH distance reaches 1.396 \AA and the HH distance is 1.412 \AA , the negative b_2 curvature disappears (see Figure 5).

(e) The $B^+ + H_2 \Rightarrow BH^+ + H$ reaction is predicted to be thermodynamically endoergic by $20\,821 \text{ cm}^{-1}$ ($20\,000 \text{ cm}^{-1}$ when zero-point corrected). In the guided ion beam experiments,^{1a} no flux of BH^+ product ions is detected for B^+ ions colliding with H_2 at kinetic energies at or slightly above this threshold; this has been used to infer that an additional activation barrier is present.

(f) A geometrically stable linear $HBH^+({}^1\Sigma_g^+)$ species is found to lie $16\,269 \text{ cm}^{-1}$ ($14\,712 \text{ cm}^{-1}$ when zero-point corrected) below $B^+ + H_2$. This species lies on the ground state 1A_1 potential energy surface and correlates with $B^+({}^1S) + H_2$ reactants when C_{2v}

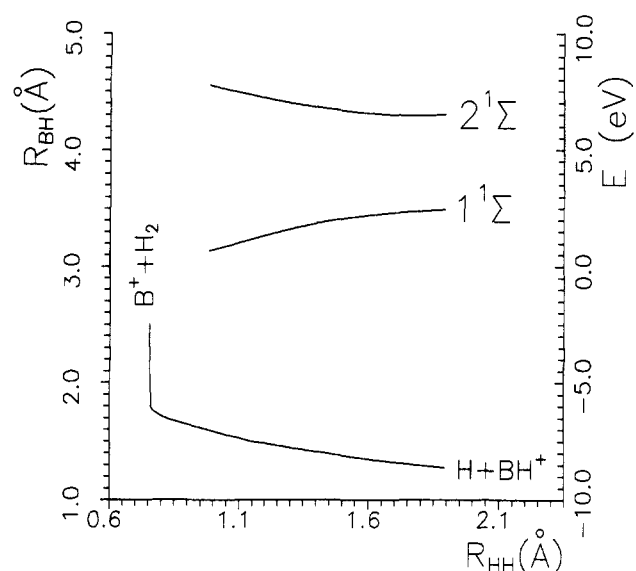


Figure 6. Reaction path for C_{2v} insertion. The lower curve gives the HH and B-to-closest-H distances along this path. The upper two curves show the lowest (${}^1\Sigma$) and first excited (${}^2\Sigma$) state energies (measured with respect to reactants $B^+ + H_2$) along this path.

symmetry is enforced (see Figure 2). Its BH bond length ($r_{BH} = 1.187 \text{ \AA}$) is only slightly shorter than that in BH^+ (1.199 \AA).

(g) Along a collinear reaction path beginning at the $B^+ + H_2$ geometry, the bending mode is unstable because of the long-range quadrupole potential. Further along the collinear approach, the bending curvatures become positive and a reaction streambed appears. Thereafter, the energy of the ${}^1\Sigma$ ground state increases monotonically and leads to $BH^+({}^2\Sigma) + H$ without any transition-state barrier; this path therefore provides the lowest energy access to $BH^+ + H$ products (see Figure 6). Near the $B^+ + HH$ entrance channel along the collinear path, the ground state is dominated by the $1\sigma^2 2\sigma^2$ configuration. The $1\sigma^2 2\sigma 3\sigma$ configuration correlates with the ground-state products $BH^+ + H$. The lack of a transition state along this reaction path is a result of the single spin–orbital occupancy difference, and thus strong coupling, between the $1\sigma^2 2\sigma^2$ and $1\sigma^2 2\sigma 3\sigma$ configurations.

(h) The first excited singlet state plays a crucial role in both the C_{2v} and collinear reaction paths. Along the C_{2v} path, its second-order Jahn–Teller coupling opens the C_2 reaction channel to yield $BH^+ + H$. This 1B_2 state has its own C_{2v} equilibrium geometry with an HH distance of 1.674 \AA and a BH distance of 1.301 \AA at which its electronic energy is $25\,852 \text{ cm}^{-1}$ above the energy of the reactants $B^+({}^1S) + H_2$. At this geometry the 1A_1 state is $12\,979 \text{ cm}^{-1}$ below the 1B_2 state. The harmonic MCSCF vibrational frequencies of the 1B_2 state are 1026 cm^{-1} (bending), 2083 cm^{-1} (symmetric stretching), and 2173 cm^{-1} (asymmetric stretching). Along the collinear path, the first excited singlet state is involved in an avoiding crossing with the ${}^1\Sigma$ ground state. In the $B^+ + HH$ entrance channel, the excited state has a $1\sigma^2 2\sigma 3\sigma$ configuration and correlates to $H_2^+ + B({}^2P)$. In the product region, this excited state has a configuration $1\sigma^2 2\sigma^2$ and describes (see Figure 3) the charge-transfer species $BH({}^1\Sigma) + H^+$.

IV. Discussion of Results and Summary

(A) **Relation to Ion Beam Experimental Data.** The most intriguing observation of the current study is that the collinear reaction path provides the lowest energy access to $BH^+ + H$. Asymptotically, collinear approaches are not geometrically favored because of the long-range quadrupole interaction which favors off-axis approaches. Only when the B^+ has approached the H_2 close enough to make the H–H distance 0.8 \AA or greater does a reaction valley appear for collinear geometries. Along this valley, the energy increases monotonically from reactants to products and no transition state appears. As a result, the reaction threshold should be equal to the thermodynamic endoenergicity, which is not consistent with the experimental findings.

On the other hand, along the C_{2v} reaction path, a point of b_2 mode instability provides access to the $BH^+ + H$ product channel. This point appears 2021 cm^{-1} above the reaction endoergicity, which matches the ion beam threshold for the production of BH^+ ions.

In the ion beam experiments, collisions take place with average relative energies^{1a} of at least 0.05 eV (400 cm^{-1}), and those that have any chance of leading to $BH^+ + H$ products have at least 20 000 cm^{-1} (2.3 eV) of relative kinetic energy. Therefore, the weak long-range attractive forces are likely to have little influence in guiding the flux of reactants toward or away from any particular orientation. In essence, collisions occur with all possible orientations; some sample regions on the potential surface near collinear geometries, others sample regions near the point of b_2 instability.

Assuming that the experimental results are correct, one is faced with explaining why the $B^+ + H_2 \Rightarrow BH^+ + H$ reaction seems to not take advantage of the lower energy collinear reaction path. We speculate at this time that, although the collinear path possesses a lower activation energy E_{coll}^* than the C_{2v} path leading to the point of b_2 instability at E_{instab}^* , the density of states available to the collinear paths is much smaller than that of the other path. As a result, collinear contributions to the overall rate of reaction are small. Stated in another manner, at the energies that characterize the guided ion beam experiments, the pre-exponential A factor associated with the collinear path is orders of magnitude smaller than that belonging to the other path.

One can estimate these paths' relative contributions to the net bimolecular reaction rate coefficient for the $B^+ + H_2 \Rightarrow BH^+ + H$ via one or another variant of transition-state theory. In such approaches, the rate coefficient k is expressed in terms of partition functions per unit volume of the B^+ and H_2 reactants as well as the activated complex associated with the particular path:

$$k = \frac{(q_{\text{BHH}}^*/V)}{(q_{\text{B}^+}/V)(q_{\text{H}_2}/V)}$$

Although we do not carry out such a detailed analysis here, we note that (i) any collinear BHH^+ activated complex has one reaction path, two rotational, and three vibrational degrees of freedom, while (ii) any nonlinear BH_2^+ activated complex has one reaction path, three rotational, and two vibrational degrees of freedom. As a result, the transition-state expression for the ratio of the rate coefficients for collinear and nonlinear paths involves

$$\frac{k_{\text{coll}}}{k_{\text{instab}}} = \frac{(q_{r1}q_{r2}q_{v1}q_{v2}q_{v3})_{\text{coll}} \exp(-E_{\text{coll}}^*/RT)}{(q_{r1}q_{r2}q_{r3}q_{v1}q_{v2})_{\text{instab}} \exp(-E_{\text{instab}}^*/RT)}$$

where the q_{r_n} denote the rotational partition functions and the q_{v_n} denote the vibrational partition functions of the respective species.

The simple fact that the rotational partition functions are at least 2 orders of magnitude larger than the vibrational partition functions (at room temperature and certainly at the energies (>2.3 eV) of the guided ion beam experiments) argues that the above ratio of rate coefficients will be approximately the ratio of a vibrational to a rotational partition function q_v/q_r , multiplied by an activation-energy factor $\exp((E_{\text{instab}}^* - E_{\text{coll}}^*)/RT)$.

According to our calculations, the energy difference $E_{\text{instab}}^* - E_{\text{coll}}^*$ is approximately 2000 cm^{-1} or ca. 0.25 eV. So, at collision energies near or above the thermodynamic threshold (ca. 2.3 eV or 20 000 cm^{-1}), the activation energy factor will be near unity: $\exp((E_{\text{instab}}^* - E_{\text{coll}}^*)/RT) = \exp(2000/20\,000) \cong 1$. At these same energies, the vibrational to rotational partition function ratio q_v/q_r is likely to be smaller than 10^{-3} . We therefore suggest that the energy range used in the ion-beam experiments allows the energetically disfavored, but density-of-states favored path to dominate. Experiments that use much lower collision energies should see a threshold equal to the endoergicity but with an A -factor (or corresponding cross-section) orders of magnitude smaller than seen in the ion-beam data.

(B) What About the Isoelectronic $Li^- + H_2 \Rightarrow LiH^- + H$ Reaction? It is interesting to speculate about another isoelectronic system: $Li^- + H_2 \Rightarrow LiH^- + H$, $HLiH^-$. For this anion, the

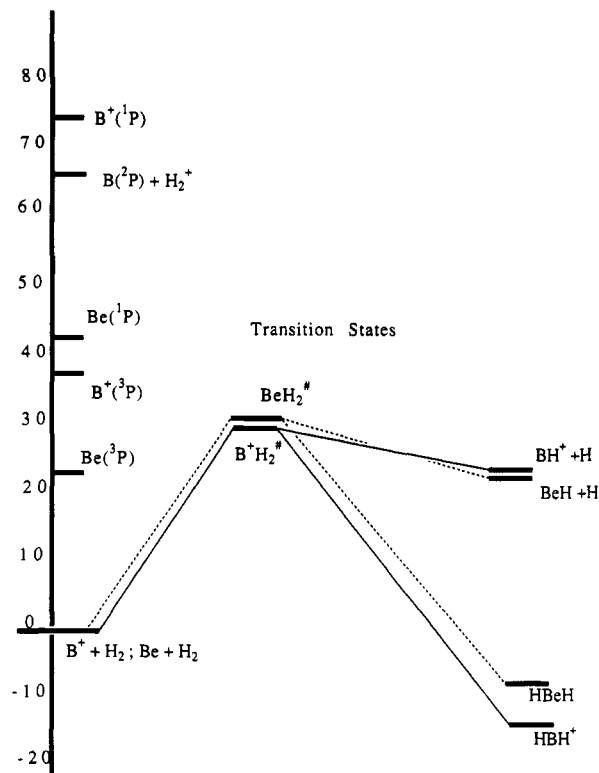


Figure 7. Diagram showing relative energies of $M + H_2$, HMH , $MH + H$, and transition states (or points of instability) for the $B^+ + H_2$ and $Be + H_2$ cases. Also shown are the locations of the $^{1,3}P$ excited states of the B^+ and Be species. All energies are in units of 1000 cm^{-1} .

long-range quadrupole and polarizability interactions both favor the collinear approach. Using the known¹² electron affinities of Li and of LiH , as well as the LiH and H_2 bond energies, one finds that $LiH^- + H$ should lie 19 100 cm^{-1} above $Li^- + H_2$. This energy difference is remarkably close to those (see Figure 7) for $B^+ + H_2 \Rightarrow BH^+ + H$ and $Be + H_2 \Rightarrow BeH + H$. The energies of the $HLiH^-$ species and of the C_{2v} or C_s transition states for the $Li^- + H_2$ reaction are not yet known, so further comparisons cannot be made.

Major differences between the Li^- case and those for B^+ and Be involve the location of the 3P excited states (see Figure 7). For B^+ and Be , the lowest of these states, the 3P state, lies 37 300 cm^{-1} and 22 000 cm^{-1} , respectively, above the 1S ground state. For Li^- , the 3P state lies higher in energy than Li (plus a free electron) and is hence metastable with respect to autodetachment. In particular, the 3P and 1P states are believed to lie between 5000 and 13 000 cm^{-1} above the 1S state, while the Li^- electron detachment energy is only 5000 cm^{-1} . The charge transfer state $X \ ^2\Sigma_u^+ + H_2^- + Li(^2S)$ is also metastable and may play a role in this system.

For the above reasons, the intersection of the 1A_1 ground-state C_{2v} surface for $Li^- + H_2$ by the excited 1B_2 surface is expected to occur at much lower energy than in the B^+ and Be cases. Moreover, the 2A_1 surface corresponding to the autodetached $Li + H_2$ species is also expected to come into play at collision energies of ca. 5000 cm^{-1} , well below even the $Li^- + H_2 \Rightarrow LiH^- + H$ reaction threshold. Therefore, qualitatively different behavior is expected both in the low-energy potential surfaces of $Li^- + H_2$ and in the guided ion beam experiments studying Li^- collisions with H_2 . It is our intention to explore this interesting case in the near future.

Before closing, it should be mentioned that there are interesting aspects of the $B^+ + H_2$ potential energy surfaces that were not addressed here because of our emphasis on the lowest singlet-state potential. In particular, the location of the 3B_2 surface in the

(12) The EA of Li is 0.62 eV Hotop, H.; Lineberger, W. C. *J. Phys. Chem. Ref. Data* 1985, 14, 731. The EA of LiH is 0.3 eV Griffing, K. M.; Kenney, J.; Simons, J.; Jordan, K. D. *J. Chem. Phys.* 1975, 63, 4073.

neighborhood of the singlet state's point of b_2 mode instability is of substantial importance to a full interpretation of the $B^+ + H_2$ reactivity data.¹³ If transitions to the 1B_2 surface play an important role, transitions to the corresponding triplet surface will also be operative. The latter events may occur with reduced probability because of the need for singlet-triplet coupling, but

they will occur at lower energy because the 3B_2 state lies below the 1B_2 state.

Acknowledgment. This work was supported in part by the Office of Naval Research and by NSF Grant CHE8814765. We acknowledge our colleague, Prof. P. B. Armentrout, for stimulating our interest in this particular system. We thank the Utah Supercomputer Institute for staff and computer resources.

Registry No. B^+ , 14594-80-0; H_2 , 1333-74-0.

(13) Hirst, D. M. *Chem. Phys. Lett.* 1983, 95, 591.

Ab Initio Study of the Molecular Structure and Vibrational Spectrum of Nitric Acid and Its Protonated Forms

Timothy J. Lee*

NASA Ames Research Center, Moffett Field, California 94035

and Julia E. Rice*

IBM Research Division, Almaden Research Center, San Jose, California 95120 (Received: July 16, 1991)

The equilibrium structure and infrared spectrum of HNO_3 (nitric acid) and its protonated forms have been determined using double- ζ plus polarization and triple- ζ plus double polarization basis sets in conjunction with several ab initio electronic structure methods. Namely, the self-consistent field (SCF), second order Møller-Plesset perturbation theory (MP2), and the single and double excitation coupled-cluster (CCSD) methods have been used. Results using the CCSD(T) method, which includes a perturbational estimate of the effects of connected triple excitations, are also presented. Accurate energy differences have been determined by computing CCSD(T) energies using large atomic natural orbital basis sets. Four different isomers of $H_2NO_3^+$ have been investigated, and it is found that the lowest energy form of protonated nitric acid corresponds to a complex between H_2O and NO_2^+ , consistent with earlier theoretical and experimental studies. There are two isomers of the complex, differing by rotation of H_2O relative to NO_2^+ , that are very close energetically ($\Delta E < 0.5$ kcal/mol), although only the planar form is found to be a minimum on the potential energy surface. The other two isomers of $H_2NO_3^+$ that have been investigated both correspond to local minima on the potential energy surface and are very close in energy. These two isomers are about 20 kcal/mol less stable than the complex. The proton affinity of nitric acid is computed to be 182.5 ± 4.0 kcal/mol, which is somewhat larger than the recent experimental estimate of Cacace et al. (168 ± 3 kcal/mol). The binding energy of the complex is determined to be 17.3 ± 2.0 kcal/mol.

1. Introduction

Nitric acid (see Figure 1) has received considerable attention recently because of its importance in atmospheric chemistry. Protonated nitric acid (Figure 2) has also been the subject of recent theoretical¹ and experimental^{2,3} studies due to its known importance in nitration reactions. Cacace et al.^{2,3} have established via metastable ion kinetic energy (MIKE) and collisionally induced dissociation (CID) spectrometry that two distinct isomers of $H_2NO_3^+$ exist in the gas phase with the lowest energy isomer corresponding to a complex between NO_2^+ and H_2O . These results are in qualitative agreement with the 1984 ab initio study of Nguyen and Hegarty¹ in which several isomers of protonated HNO_3 were investigated using the self-consistent field (SCF) level of theory together with the 4-31G and 6-31G** basis sets. Nguyen and Hegarty found that the most stable isomer of $H_2NO_3^+$ (II) was a complex between NO_2^+ and H_2O , while two other isomers of $H_2NO_3^+$ (IV and V) were about 8-10 kcal/mol higher in energy. An additional isomer (not pictured) was found to be about 22 kcal/mol less stable than II, which may be expected due to the close proximity of the hydrogen atoms. By today's standards the equilibrium structure of HNO_3 obtained by Nguyen and Hegarty is not in very good agreement with the experimental

structure,⁴ although given the level of theory used, the agreement is reasonable. The only other computed property which could be compared with experiment is the barrier height for rotation of the O-H group (about the N-O bond) relative to the NO_2 group in nitric acid. This quantity was computed to be 9.2 kcal/mol, without the effects of zero-point vibrational energy, which is in good agreement with the most recent experimental estimate (7.8 kcal/mol⁵).

The proton affinity of HNO_3 was also determined in the ab initio study¹ (180 kcal/mol, again neglecting zero-point vibrational energies), but an experimental estimate of this quantity was unavailable. Although Cacace et al.^{2,3} were unable to measure the gas-phase proton affinity of HNO_3 directly, they were able to estimate a value of 168 ± 3 kcal/mol based upon a bracketing technique. That is, the proton affinity of nitric acid was determined to be between that of H_2O (166 kcal/mol⁶) and CF_3C-H_2OH (169 kcal/mol⁷). It is certainly within the capabilities of present day ab initio quantum mechanical methodology to determine this proton affinity to within a few kcal/mol, thereby determining the reliability of the estimate of Cacace et al. Given the number of unreliable experimental proton affinity measurements (see for example ref 8) and the fact that Cacace et al. were

(1) Nguyen, M.-T.; Hegarty, A. F. *J. Chem. Soc., Perkin Trans. 2* 1984, 2043.

(2) Cacace, F.; Attina, M.; de Petris, G.; Speranza, M. *J. Am. Chem. Soc.* 1989, 111, 5481.

(3) Cacace, F.; Attina, M.; de Petris, G.; Speranza, M. *J. Am. Chem. Soc.* 1990, 112, 1014.

(4) Cox, A. P.; Riveros, J. M. *J. Chem. Phys.* 1965, 42, 3106.

(5) McGraw, G. E.; Bernitt, D. L.; Hisatsune, I. C. *J. Chem. Phys.* 1965, 42, 237.

(6) Lias, S. G.; Bartmess, J. E.; Liebman, J. F.; Holmes, J. L.; Levin, R. D.; Mallard, W. G. *J. Phys. Chem. Ref. Data* 1988, 17, Suppl. 1.

(7) See ref 6 in ref 3.